Hygrothermal aging and structural damage of a jute/poly (lactic acid) (PLA) composite observed by X-ray tomography[1]

Ning Jiang[a,b,c,*], Tao Yu[a,d,*], Yan Li[a], Talha J Pirzada[b], Thomas James Marrow[b,*]

a *School of Aerospace Engineering and Applied Mechanics, Tongji University, 1239 Siping Road, Shanghai 200092, PR China*

b *Department of Materials, University of Oxford, Parks Road, Oxford OX1 3PH, United Kingdom*

c *School of Transportation and Vehicle Engineering, Shandong University of Technology, Zibo 255049, PR China*

d *State Key Laboratory for Strength and Vibration of Mechanical Structures, Xi'an Jiaotong University, Xi'an 710049, PR China*

*Corresponding Authors:

Prof. Tao Yu, E-mail: yutao@tongji.edu.cn. Phone: +86-21-65980239

Prof. Thomas James Marrow, E-mail: james.marrow@materials.ox.ac.uk. Phone: +44-1865-273938

Dr. Ning Jiang, E-mail: jiangning@sdut.edu.cn. Phone: +86-15221778806

Abstract

Biodegradable plant fiber reinforced poly (lactic acid) (PLA) composites are potential replacements for traditional synthetic fiber reinforced composites. These may experience hygrothermal aging from the combined effects of moisture and heat. The effects of aging in water at 50°C on water absorption, chemical degradation of the fibers and matrix, and the tensile properties of a jute fiber/PLA composite have been correlated with changes in the internal structure, observed by high-resolution computed

[1] This is the authors' copy of a paper accepted for publication in the journal Composite Science and Technology https://doi.org/10.1016/j.compscitech.2019.01.018

X-ray tomography. Water absorption during aging causes fiber/matrix interface failure and then matrix embrittlement, and these are detrimental to the tensile strength, stiffness and ductility.

Keywords: A. Short-fibre composites; B. Environmental degradation; B. Mechanical properties; B. Porosity; C. Damage mechanics

1 Introduction

There is a growing interest in substituting non-biodegradable, petroleum-based polymers and composites with 'green' or renewable materials to address the problems of oil-resource depletion and environmental pollution[1-3]. Due to advantageous characteristics[4-6] that include biodegradability, good mechanical properties and low density, plant fiber/poly(lactic acid) (PLA) composites offer an sustainable alternative to conventional composites. Their potential uses include lightweight components in aerospace and automobile applications, such as door trim, panels and seat, which require sufficient mechanical strength to fulfill their function and may be exposed to hygrothermal environments (i.e. combination of moisture and heat). It is important to understand how ageing affects these composites, as it may limit their service life.

Various chemical and physical processes (i.e. plasticizing, swelling, and hydrolysis) may occur during hygrothermal aging[7-10]. There are three different paths for moisture transportation in plant fiber reinforced composites: 1) transport by lumens in the plant fibers; 2) capillary action along the interface between fiber and matrix; and 3)

diffusion through the matrix[11, 12]. Moisture can disrupt the bonding between the fiber and matrix, leading to a poor interface, and moisture absorption can also cause differential swelling, which develops stresses that can cause fracture of the matrix[13]. Moreover, moisture promotes hydrolysis of the PLA due to cleavage of –C–O– ester bond. This embrittles the matrix, and the consequent microcracking may catalyze further degradation of the composite by macrocracks[14], increased water absorption[15], and delamination[16, 17]. All of those can be detrimental to the material's strength, stiffness and dimensional stability[14, 15, 18, 19].

The aging behaviors of plant fiber/PLA composites have been reported by several authors, and although the effects of water absorption on the chemical and physical properties are broadly understood, there are no high-fidelity observations of the internal voids and cracks that can affect the mechanical properties of plant fiber/PLA composites after aging. Void geometry and location have a strong influence on the properties of composites [20], so it is important to understand their development. Hence, the aim of this investigation was to observe the internal structure of a plant fiber/PLA composite at different aging stages in order to clearly establish the relationship between the structure and mechanical properties.

Internal damage in composites, such as weak interfaces and cracks, can be extremely difficult to detect and quantify, and various techniques have been used to date. For example, David et al.[21] showed that the 'tap' test, which is a form of instrumented impact test, can be used as a quantitative low resolution imaging tool for composites structures on aircraft. Kinra et al.[22] detected matrix cracks in laminated composites

by an ultrasonic backscattering technique, which could also be used to assess the depth and location of flaws[23, 24]. More generally, surface microscopy, such as scanning electron microscopy (SEM), is widely applied to study the internal structure of composites[10, 25-29]. However, the specimens are destroyed when two-dimensional imaging techniques are used to study internal features such as cracks and voids, and they also provide quite limited information on 3-dimensional structures.

X-ray computed tomography is a non-destructive, high-resolution technique that can study the internal structural details of materials. The obtained image is essentially a three-dimensional map of the X-ray linear attenuation coefficient. It allows 3D visualization and quantitative analysis of the microstructure, such as the spatial distribution of features and phases and their volume fractions. Many studies have used X-ray tomography to characterize damage and internal flaws in composites, and in situ observations can examine their progressive development with time or loading. As examples: Schilling et al.[30] used X-ray tomography to characterize damage and internal flaws, including delamination and microcracking, in a mechanically loaded glass/epoxy and graphite/epoxy composites; Firas et al.[31] applied X-ray tomography to evaluate the effects of accelerated thermal degradation, observing reinforcement filler damage, material homogeneities, cracking and microcracking in epoxy resin composites. Saucedo-Mora et al.[32] and Wan et al.[33] monitored the evolution of damage in ceramic fiber reinforced ceramic matrix composites, using digital volume correlation of X-ray tomographs to quantify the deformation and as an aid to crack visualization.

In this study, X-ray tomography has been used for the first time to characterize the internal structure of a jute/PLA composite that had been subjected to hygrothermal aging. The objective was to understand how this was related to the observed changes in the composite's mechanical properties.

2 Experimental

2.1 Materials

The poly(lactic acid) (PLA) (4032D, molecular weight $\overline{M}_w$=150,000) was obtained from the Suzhou Jiwang Environmentally Friendly Material Co. Ltd (China). It had a D stereo-isomer content of about 1.5%. The jute fiber yarns were obtained from the Shanghai Qiancong Jute Fiber Co. Ltd. (China).

Prior to processing, PLA granules and cut jute fiber yarns (~4 cm fiber length) were dried under vacuum at 80ºC for 4 hours. Compounding of the PLA and jute fiber was performed in a SHJ-20 twin-screw extruder (Nanjing Jieya Co. Ltd, China, screw diameter = 27 mm, screw speed = 100 rpm, feed rate=30 g/min, length to diameter ratio = 40, co-rotating screws). The extrusion temperature was independently controlled over seven zones (160, 165, 165, 170, 170, 165, and 160°C) from the feed zone to the exit die. After compounding, the jute/PLA material was granulated and dried again under vacuum at 80ºC for 4 hours. The weight fraction of jute fiber in the composite granules was 10%. The dry density of jute fiber[34] is reported to be the range of 1.350 to 1.490 g cm^{-3}, compared with ~1.25 g cm^{-3} for PLA[35], so the volume fraction of jute fiber is expected to be in the range 8.5% to 9.3%.

The test specimens were prepared from the compounded jute/PLA using a PL550/150 injection-moulding machine (Wuxi Haitian Machinery Co. Ltd, China). The hopper temperature was 90°C, the temperature profile from feed to exit was 175, 180, 180 and 175°C, and the injection pressure was 55 Bar.

2.2 Hygrothermal Aging

Aging under hygrothermal conditions were carried out in a test chamber filled with deionized water that was maintained at 50ºC. Before aging, the specimens were dried in air for 24 hours at 40ºC. The specimens were immersed in the water and removed for characterization after the specified aging times. The amount of water, relative to the volume of the dry specimens, was fixed at the ratio 100:1.

2.3 Characterization

2.3.1 Water Absorption and FTIR

The water absorption test specimens (30 mm × 20 mm × 4 mm) were weighed to determine their initial weight (W_0) using a high precision balance (Precisa-XR, Switzerland, precision=10^{-4} g). The weight (W_t) was recorded at each periodic removal of the specimen, and the weight gain (M_t, %) was calculated with equation (1). Five specimens were tested to obtain the average and standard deviation. The weight of a typical sample prior to water absorption was 3.7 g.

$$M_t = \frac{W_t - W_0}{W_0} \times 100 \qquad (1)$$

Fourier transform infrared (FTIR) spectra of the soak solution were recorded using a NEXUS670 spectrometer (Thermofisher, USA) in the mid-infrared range of 800-4000 cm^{-1}.

2.3.2 Tensile Tests

Tensile properties were measured using a WHY-W mechanical testing machine (Chengde Instruments co. Ltd., China), according to the ASTM D3039 standard with a cross-head speed of 2 mm min^{-1}. Five specimens were tested for each aging time. The parallel-sided section was 90 mm long, 10 mm wide and 4 mm thick (**Error! Reference source not found.**), so the strain rate was approximately 4×10^{-4} s^{-1}. An extensometer (50 mm gauge length) measured the longitudinal strain.

2.3.3 Fractography

Impact tests, to obtain fracture surfaces, were done using a XCJ-50 test machine (Chengde test instrument Ltd., China), with specimens that were $80 \times 10 \times 4$ mm^3 in size[36]. The fracture surfaces were observed by SEM (Quanta 250 FEG, FEI Ltd., USA) at room temperature with an accelerating voltage of 15 kV. Prior to observation, the surfaces were gold coated using a vacuum sputter coater.

2.3.4 X-ray Computed Tomography

Computed tomographs were obtained using an X-ray microscope (Xradia 510 Versa, Zeiss, Germany). The cuboid samples were nominally 4 mm × 6 mm × 4 mm in size, and were cut from the center of tensile specimens that had not been mechanically loaded. X-ray tomography allows non-destructive observation of the microstructure, so any damage observed could be directly attributed to the hygrothermal degradation with no

effect of specimen preparation. The tomographed volume, relative to the specimen, is shown in **Error! Reference source not found.**. Observations were obtained at a voxel size of 3 μm (medium resolution, MR) and 1 μm (high resolution, HR). Each tomograph was reconstructed from 1601 projections collected over a 180° rotation with a 4× objective and 2× binning with the 2048 × 2048 pixel CCD detector (i.e. to obtain a 1024 × 1024 × 1024 voxel 3D dataset). The optimized conditions, setup and durations for the tomographs are summarized in **Error! Reference source not found.**. Depending on these, the microstructures were imaged within a cylindrical region with length and diameter of ~3 mm (MR) or ~1 mm (HR).

Visualization and quantitative analysis of the tomographs were done using Avizo 9.0 software (Visualization Sciences Group, Bordeaux, France). After noise reduction by 3D median filtering, image intensity thresholding was applied to identify and segment the fibers, matrix and the porosity. Each voxel forming the 3D picture measures a grey level which corresponds to the X-ray attenuation coefficient of the represented matter. The X-ray attenuation coefficient depends on electron density [37], which for this material and scanning energy, is closely related to density. So, it can be used to identify whether the voxel contains mostly fiber, matrix or is empty (i.e. crack or void). To process the tomography data, thresholds that allow one to separate the different phases must be chosen. This is a choice, which depends on the level of contrast and image resolution, as voxels that contain two phases will have an intermediate intensity (i.e. partial volume effect). The sensitivity of the segmentation of porosity is illustrated in Figure 2, which shows that thresholds chosen between 80-100 in the 256 greyscale

range reproducibly separate the pores from the matrix. This shows the tomograph has sufficient contrast to define the observable pores. The chosen segmentation threshold was within this range, and the uncertainty in pore volume fraction is estimated to be ~0.1%, using the standard deviation in the plateau region around the chosen threshold. The jute fibers and PLA matrix were identified and segmented by the same method.

3 Results and Discussion

3.1 Water Absorption and Tensile Properties

Three stages of aging are apparent from the measured weight gain (M_t) and tensile strength (Figure 3a). Water absorption increased rapidly in the first 7 days (stage I), but with a small decrease of tensile strength. The strain at failure increased and the tensile elastic modulus decreased (**Error! Reference source not found.**c). This is due to the plasticizing effect of water molecules[38], and such changes in mechanical properties have been reported to be reversible[39]. The linear relationship between M_t and $t^{1/2}$ in stage I (Figure 3b) indicates that the water absorption of jute/PLA composites followed Fickian behavior[36, 40], whereby water diffused into the microstructure without any observable physical change or chemical reaction. This is supported by the FTIR data (**Error! Reference source not found.**) and SEM observations (**Error! Reference source not found.**a); in comparison to deionized water, the FTIR spectrum of the soak solution after 7 days shows no additional peaks that would indicate a chemical reaction, and the SEM observations of the fracture surfaces of impact specimens show no

tendency for weakness between the jute fiber and PLA matrix that would indicate a change in interface properties.

Between 7 to 28 days (Stage II), the weight increased more slowly without saturation. This deviation from Fickian behavior[41] was accompanied by the development of a weak interface between fiber and matrix, which is indicated by SEM observation of interfacial failures (**Error! Reference source not found.**b). This is due to the capacity for water absorption and swelling of natural fibers and the PLA matrix[13]. Damage at the interface led to further water absorption and a decline in the composite's tensile strength and tensile elastic modulus. In stage III (28~56 days), cracking of the PLA matrix (**Error! Reference source not found.**c) increased the rate of water absorption and also decreased the tensile strength and elastic modulus; little ductility (i.e. strain to failure) of the composite remained at this stage.

In the corresponding soak solutions, FTIR peaks were found at 1186 cm^{-1}, 1100 cm^{-1} and 1062 cm^{-1} at 42 days (**Error! Reference source not found.**). These can be assigned to stretching of C-O in PLA (1186 cm^{-1}) and C-O-C (1100 cm^{-1}) and C-O (1062 cm^{-1}) in cellulose[42], which is present in jute fibers. The peak at 1186 cm^{-1} shows that significant amounts of PLA oligomer have diffused into deionized water after aging. In addition, for the jute/PLA soaked solution, characteristic peaks at about 1100 cm^{-1} and 1062 cm^{-1} illustrates the effects of the cellulose hydrolyzation and transport of the hydrolyzates into the soak solution. From these results, it can be concluded that both PLA and jute fibers underwent degradation during stage III.

3.2 Microstructure and Damage Characterisation

3.2.1 Initial Microstructure

The tomographic images (**Error! Reference source not found.**) show the microstructure of the unaged composite. The X-ray attenuation coefficient of the jute fiber is slightly higher than the matrix, as the fibers appear lighter in contrast, and this allows segmentation via an image intensity threshold (**Error! Reference source not found.**b and c). Visual inspection indicates that the fibers are well dispersed, which indicates that jute fibers had good wettability in the PLA matrix. The internal porosity of the fibers is resolved, but there are almost no pores (i.e. voids) observed at the fiber/matrix interface, nor in the matrix, demonstrating a good interface between jute fiber and PLA matrix (**Error! Reference source not found.**d). Using image segmentation, the volume fractions of fibers and pores are 8.6% and 0.05%, respectively; the fiber volume fraction is consistent with the expected quantity (8.5%~9.3%) from manufacture and the negligible porosity is at the level of the uncertainty in the porosity segmentation. The average length of the fibers is 300 μm (standard deviation 177 μm), as they have been reduced in length by the action of the twin-extruder.

By inspection, the fibers tend to be aligned with the mould flow direction (i.e. X-direction defined in **Error! Reference source not found.**). This is confirmed by quantitative analysis of the orientations of the Euler angles of the fibers, using the skeletonization algorithm of the Avizo software, applied after segmentation of the tomography data (**Error! Reference source not found.**e and f). The polar angles *(θ)* of

74% of the fibers are within 20º of the XY plane, and close to 70% have their azimuthal angle (φ) within 30° of the X-direction. This preferential alignment is due to the high shear in the flow direction during moulding.

3.2.2 Effects of Aging

Tomography (**Error! Reference source not found.**) allows comparison of the characteristic microstructures that are observed in stages I to III. At 7 days (stage I) (**Error! Reference source not found.**b), there is no visible difference from the unaged microstructure (Figure 7a). However, at 21 days (stage II), increased porosity is observed (**Error! Reference source not found.**c), and this increases significantly by 42 days (stage III) (**Error! Reference source not found.**d). The tomography at stage II (e.g. after 21 days aging, **Error! Reference source not found.**c) shows the first cracking is at the interface between the jute fibers and matrix. This is consistent with previous destructive observations[39] that used SEM to study the effects of hydrothermal aging.

The cracks can be measured as porosity. The average porosity at stage II is 1.8%, which is significantly higher than the 0.32% porosity observed at stage I. The average fiber volume fraction measured at stage II is 8.1%, compared to 8.4% at stage I and to 8.6% prior to aging. A tomograph of a stage II specimen is shown in **Error! Reference source not found.**a. Its fiber and porosity fractions were measured as the area fractions in 2D slices, which were taken orthogonally at intervals of 3 μm in a cube volume at its center. There is a clear relationship between the porosity and fiber fraction (**Error! Reference source not found.**b, c, d), with higher porosity observed in slices that

intersect a greater fraction of fibers. The correlation between fiber fraction and porosity is strongest for the YZ plane, which is perpendicular to the moulding direction (**Error! Reference source not found.**e).

3D rendering of the fibers and porosity (**Error! Reference source not found.**) confirms that the voids have formed around the jute fibers. The correlation between fiber fraction and porosity is strongest in the YZ plane due to the alignment of the jute fibers parallel to the X-axis that was caused by flow. Sectioning perpendicular to the fibers therefore provides more consistent observations of the voids than sections that are oriented nearly parallel to the fibers. The partial volume effect (i.e. voxels that contain both fiber and pores) causes the apparent decrease in fiber fraction with aging as the number of pores increases, as there is a high proportion of voxels at the pore/fiber interface.

Tomographs of stage III samples, aged for 42 days, (**Error! Reference source not found.**d and **Error! Reference source not found.**a-d) show significant cracking of the PLA matrix. The spatial variation of porosity (i.e. cracks) (**Error! Reference source not found.**e) is quite uniform with distance in the X and Y directions, while there is an increase in porosity towards the surface of the specimen; the Z-axis is across the thickness of the specimen, and the center of the tomographed volume, at the 400 μm coordinate, is positioned at 300 μm from the surface. Damage in the PLA matrix, which is weakened by hydrolysis, may be greatest close to the surface due to the longer water absorption time, as water enters via the connected network of microcracks. This may be investigated in future studies that could use in situ observations of damage by

repeated X-ray tomography to quantify the time dependence of damage by hygrothermal action, and so characterise the kinetics of water penetration.

3.3 Microstructure Effects on the Mechanical Properties

The porosity increases as a function of aging time (**Error! Reference source not found.**a) and is accompanied by a detrimental effect on tensile strength (**Error! Reference source not found.**b). In stage I (0 to 7 days), the tensile strength declines (<12%) with a small change in porosity (<0.27% volume fraction) and a 16% decrease in tensile elastic modulus from 4.8 GPa to 4.1 GPa (**Error! Reference source not found.**), although the strain to failure increases from 1.4% to 2.3%. Aging in stage I causes no observable damage (**Error! Reference source not found.**), so the change in mechanical properties is attributed to plastication[38] by the absorbed water molecules, which reduces the strength and modulus of the PLA and increases the composite's ductility.

The tensile elastic modulus declined to 3.6 GPa (>25% change relative to the unaged condition) in stage II (7 to 28 days) as the porosity increased substantially to 1.8%. The porosity, localized at the interface between the jute fiber and PLA matrix (**Error! Reference source not found.**), directly reduced the efficiency of stress transfer between fiber and matrix. The failure of the interface introduced cracks that reduced the tensile strength and strain to failure. In stage III (>28 days), the porosity increased further due to hydrolysis of the PLA matrix that caused embrittlement and internal cracking, which significantly reduced the strain to failure.

4 Conclusion

The effects of hygrothermal degradation on the microstructure of a jute fiber/PLA composite can be quantified for the first time by X-ray tomography. Three degradation stages of hygrothermal aging of jute/PLA composites are observed and can be related to the changes in mechanical properties. In stage I, plastication from water absorption increases the ductility with a reduction in strength and tensile elastic modulus (stage I) without an observable change in microstructure. In stage II, cracking between the fiber and matrix due to differential swelling and weakening of the interface has a significant detrimental effect on the mechanical properties. In stage III, hydrolysis of the matrix causes microcracking with a further significant decrease in ductility.

Acknowledgments

This work is supported by the graduate school of Tongji University, Ministry of Industry and Information Technology of China (MJ-2015-H-G-103), Program of Shanghai Academic Research leader (No. 16XD1402900), the Fund of State Key Laboratory for Strength and Vibration of Mechanical Structures (Xi'an Jiaotong University). EPSRC Grant EP/M02833X/1 "University of Oxford: experimental equipment upgrade" supported the Xradia Versa 510 microscope and facilities for data analysis and visualization.

References

[1] Siracusa V, Rocculi P, Romani S, Rosa MD. Biodegradable polymers for food packaging: a review. Trends in Food Science & Technology. 2009;19(12):634-643.

[2] Yu L, Dean K, Li L. Polymer blends and composites from renewable resources. Progress in Polymer Science. 2006;31(6):576-602.

[3] Moustafa H, Kissi NE, Aboukandil AI, Abdelaziz MS, Dufresne A. PLA/PBAT bionanocomposites with antimicrobial natural rosin for green packaging. ACS Applied Materials & Interfaces. 2017;9(23):20132.

[4] Taib RM, Ramarad S, Ishak ZAM, Todo M. Properties of kenaf fiber/polylactic acid biocomposites plasticized with polyethylene glycol. Polymer Composites. 2010;31(7):1213-1222.

[5] Lee SH, Ohkita T, Kitagawa K. Eco-composite from poly(lactic acid) and bamboo fiber. Holzforschung. 2004;89(9):2888-2536.

[6] Bax B, Müssig J. Impact and tensile properties of PLA/Cordenka and PLA/flax composites. Composites Science & Technology. 2011;68(7):1601-1607.

[7] Thwe M, Liao K. Durability of bamboo-glass fiber reinforced polymer matrix hybrid composites. Composites Science and Technology. 2003;63(3):375-387.

[8] Joseph PV, Rabello MS, Mattoso LHC, Joseph K, Thomas S. Environmental effects on the degradation behaviour of sisal fibre reinforced polypropylene composites. Composites Science & Technology. 2002;62(10–11):1357-1372.

[9] Gil-Castell O, Badia JD, Kittikorn T, Strömberg E, Martínez-Felipe A, Ek M, et al. Hydrothermal ageing of polylactide/sisal biocomposites. Studies of water absorption behaviour and Physico-Chemical performance. Polymer Degradation & Stability. 2014;108:212-222.

[10] Spiridon I, Leluk K, Resmerita AM, Darie RN. Evaluation of PLA–lignin bioplastics properties before and after accelerated weathering. Composites Part B Engineering. 2015;69:342-349.

[11] Robert M, Roy R, Benmokrane B. Environmental effects on glass fiber reinforced polypropylene thermoplastic composite laminate for structural applications. Polymer Composites. 2010;31(4):604-611.

[12] Wang W, Sain M, Cooper PA. Study of moisture absorption in natural fiber plastic composites. Composites Science & Technology. 2006;66(3):379-386.

[13] Almgren KM, Gamstedt EK, Berthold F, Lindström M. Moisture uptake and hygroexpansion of wood fiber composite materials with polylactide and polypropylene matrix materials. Polymer Composites. 2010;30(12):1809-1816.

[14] Dry C. Procedures developed for self-repair of polymer matrix composite materials. Composite Structures. 1996;35(3):263-269.

[15] Pang JWC, Bond IP. A hollow fibre reinforced polymer composite encompassing self-healing and enhanced damage visibility. Composites Science & Technology. 2005;65(11):1791-1799.

[16] Dittenber DB, Gangarao HVS. Critical review of recent publications on use of natural composites in infrastructure. Composites Part A Applied Science & Manufacturing. 2012;43(8):1419-1429.

[17] Araújo JR, Waldman WR, Paoli MAD. Thermal properties of high density polyethylene composites with natural fibres: Coupling agent effect. Polymer Degradation and Stability. 2008;93(10):1770-1775.

[18] Thwe MM, Liao K. Effects of environmental aging on the mechanical properties of bamboo–glass fiber reinforced polymer matrix hybrid composites. Composites Part A Applied Science & Manufacturing. 2002;33(1):43-52.

[19] Nairn JA. Matrix microcracking in composites. Polymer Matrix Composites. 2001;(04):403–432.

[20] Huang H, Talreja R. Effects of void geometry on elastic properties of unidirectional fiber reinforced composites. Composites Science & Technology. 2005;65(13):1964-1981.

[21] Hsu DK, Barnard DJ, Peters JJ, Dayal V. Physical basis of tap test as a quantitative imaging tool for composite structures on aircraft. 2000;509:1857-1864.

[22] Kinra VK, Ganpatye AS, Maslov K. Ultrasonic Ply-by-Ply detection of matrix cracks in laminated composites. Journal of Nondestructive Evaluation. 2006;25(1):37-49.

[23] Achenbach JD, Rajapakse Y, Gautesen AK. Solid mechanics research for quantitative non-destructive evaluation. Journal of Applied Mechanics. 1987;55(1):252-253.

[24] Seviaryna I, Bueno HG, Maeva E, Tjong J. Characterization of natural fibre-reinforced composites with advanced ultrasonic techniques. Ultrasonics Symposium, 2014:1428-1431.

[25] Sato N, Kurauchi T, Sato S, Kamigaito O. SEM observations of the initiation and propagation of cracks in a short fibre-reinforced thermoplastic composite under stress. Journal of Materials Science Letters. 1983;2(5):188-190.

[26] Lee WJ, Clancy AJ, Kontturi E, Bismarck A, Shaffer MS. Strong and stiff: high-performance cellulose nanocrystal/poly(vinyl alcohol) composite fibers. Acs Applied Materials & Interfaces. 2016;8(46):31500.

[27] Tu S, Zhu C, Zhang L, Wang H, Du Q. Pore Structure of macroporous polymers using polystyrene/silica composite particles as pickering stabilizers. Langmuir the Acs Journal of Surfaces & Colloids. 2016;32(49):13159.

[28] Yu T, Jiang N, Li Y. Study on short ramie fiber/poly(lactic acid) composites compatibilized by maleic anhydride. Composites Part A Applied Science & Manufacturing. 2014;64(21):139-146.

[29] Dong P, Chipara AC, Loya P, Yang Y, Ge L, Lei S, Li B, Brunetto G, Machado LD, Hong, L. A solid-liquid self-adaptive polymeric composite. ACS applied materials & interfaces. 2016;8(3):2142.

[30] Schilling PJ, Karedla BPR, Tatiparthi AK, Verges MA, Herrington PD. X-ray computed microtomography of internal damage in fiber reinforced polymer matrix composites. Composites Science & Technology. 2005;65(14):2071-2078.

[31] Awaja F, Arhatari B, Wiesauer K, Leiss E, Stifter D. An investigation of the accelerated thermal degradation of different epoxy resin composites using X-ray microcomputed tomography and optical coherence tomography. Polymer Degradation & Stability. 2009;94(10):1814-1824.

[32] Saucedo-Mora L, Lowe T, Zhao S, Lee PD, Mummery PM, Marrow TJ. In situ observation of mechanical damage within a SiC-SiC ceramic matrix composite. Journal of Nuclear Materials. 2016;481:13-23.

[33] Fratzl P, Weinkamer R. Nature's hierarchical materials. Progress in Materials Science. 2007;52(8):1263-1334.

[34] Chakravarty AC. Measurement of density of fibers of jute by density gradient column. Journal of Polymer Science Part A Polymer Chemistry. 2010;54(160).

[35] Farah S, Anderson DG, Langer R. Physical and mechanical properties of PLA, and their functions in widespread applications - A comprehensive review. Advanced Drug Delivery Reviews. 2016;107:367.

[36] Jiang N, Yu T, Li Y. Effect of hydrothermal aging on injection molded short jute fiber reinforced poly(lactic acid) (PLA) composites. Journal of Polymers & the Environment. 2018;26:3176-3186.

[37] Baruchel J , Buffiere JY , Maire E. X-ray tomography in material science. 2000, pp. 204.

[38] Almgren KM, Akerholm M, Gamstedt E K, Salmen L, Lindstrom, M. Effects of moisture on dynamic mechanical properties of wood fiber composites dtudied by dynamic FT-IR spectroscopy. Journal of Reinforced Plastics & Composites, 2008;27(16-17):1709-1721.

[39] Regazzi A, Cornauthor S. Reversible and irreversible changes in physical and mechanical properties of biocomposites during hydrothermal aging. Industrial Crops & Products. 2016;84:358-365.

[40] Shen CH, Springer GS. Moisture absorption and desorption of composite materials. Journal of Composite Materials. 1976;10(1):2-20.

[41] Weitsman YJ. Anomalous fluid sorption in polymeric composites and its relation to fluid-induced damage. Composites Part A Applied Science & Manufacturing. 2006;37(4):617-623.

[42] Cai M, Takagi H, Nakagaito AN, Katoh M, Ueki T, Waterhouse GIN, Li Y. Influence of alkali treatment on internal microstructure and tensile properties of abaca fibers. Industrial Crops & Products. 2015;65:27-35.

Captions

Figures

Figure 1: Geometry of tensile specimens and the location and orientation of the tomographed volume. The extrusion direction (i.e. mould flow direction) is along the tensile specimen axis (X-direction).

Figure 2: Effect of threshold choice on measured porosity (example: aged 42 days).

Figure 3: (a) Tensile strength and weight gain (Mt) of the jute/PLA composite with aging time (error bars are one standard deviation from 5 measurements). (b) Example stress versus strain data from individual tests at different aging times.

Figure 4: FTIR absorbance spectra of the soak solution after different aging times. Characteristic peaks from C-O and C-O-C bonds are observed at 42 days.

Figure 5: Impact fracture surfaces, observed by SEM: (a) no aging; (b) aged for 21 days (stage II); (c) aged for 42 days (stage III).

Figure 6: Tomography of the unaged composite: (a) 3D dimensional view, observed at medium resolution (MR); (b) Segmentation of fibers from the matrix by applying an intensity threshold; (c) 3D volume rendering of segmented fibers; (d) Example of high resolution tomographs (HR) of the composite. The orientation distributions of the fibers (polar coordinates) are summarized in (e) polar angle, θ; and (f) azimuthal angle, φ.

Figure 7: Example sections of medium resolution tomographs (MR) of the composite after (a) 0 day (un-aged); (b) 7 days (stage I); (c) 21 days (stage II) and (d) 42 days (stage III) aging.

Figure 8: Quantitative analysis of the composite microstructure after aging 21 days (stage II): (a) 3D dimensional view (MR tomograph)); (b), (c) and (d) show the fraction of fiber and porosity (measured in a HR tomograph) in as a function of the distance along the orthogonal X, Y, Z directions; (e) the relationship between fiber fraction and porosity in the orthogonal planes (XZ, XY, YZ).

Figure 9: Distribution of voids and fibers in the composite after aging 21 days (stage II): (a) 3D dimensional view (HR tomograph) with fibers and cracks labeled; (b) image segmentation by contrast threshold to identify voids (cracks); (c) 3D rendering of segmented fibers and cracks; (d) 3D rendering of fibers only.

Figure 10: High resolution (HR) tomography of the composite after aging 42 days (stage III): (a) YZ slice; (b) YZ slice with image segmentation to identify the cracks; (c) XY slice with fibers outlined; (d) 3D visualization and the image segmentation to show cracks; (e) Measured porosity as a function of distance in the three orthogonal directions in the same volume.

Figure 11: The variation of: (a) measured porosity as a function of aging time; (b) tensile strength as a function of porosity.

Tables

Table 1: Instrument parameters used for Medium (MR) and High (HR) resolution imaging by X-ray tomography

Table 2: Measured porosity of the tomographed specimens, and the average tensile strength, elastic modulus and strain to failure of jute/PLA composites, with aging time. The standard deviations (in brackets) are from 5 measurements of the mechanical properties.

Tables

Table 1: Instrument parameters used for Medium (MR) and High (HR) resolution imaging by X-ray tomography

Category	MR	HR
Voltage (kV)	80	60
Power (W)	7	5
Source to sample distance (mm)	40	37
Detector to sample distance (mm)	50	209
Exposure time per radiograph (s)	3	15
Pixel size (μm)	3	1
Total scanning time (hours)	3	8

Table 2: Measured porosity of the tomographed specimens, and the average tensile strength, elastic modulus and strain to failure of jute/PLA composites, with aging time. The standard deviations (in brackets) are from 5 measurements of the mechanical properties.

Aging time (Days)	0	7	21	28

Porosity (%)	0.05	0.32	1.81	2.45
Tensile strength (MPa)	58.12 (2.13)	49.72 (0.25)	30.18 (0.95)	12.60 (1.18)
Elastic modulus (GPa)	4.82 (0.09)	4.05 (0.15)	3.61 (0.04)	3.55 (0.05)
Strain to failure (%)	1.42 (0.02)	2.30 (0.17)	1.75 (0.11)	0.33 (0.06)

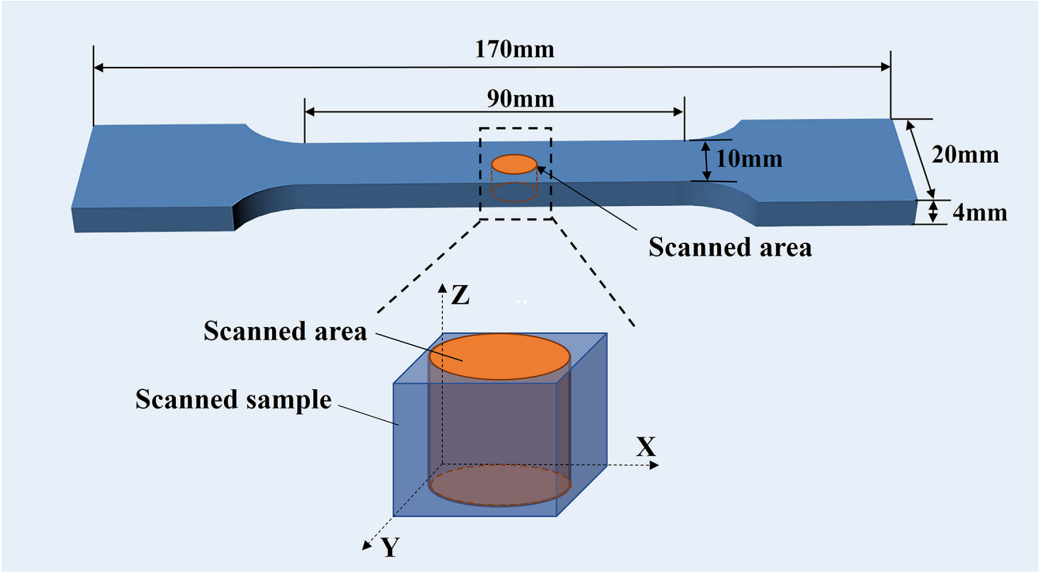

Figure 1

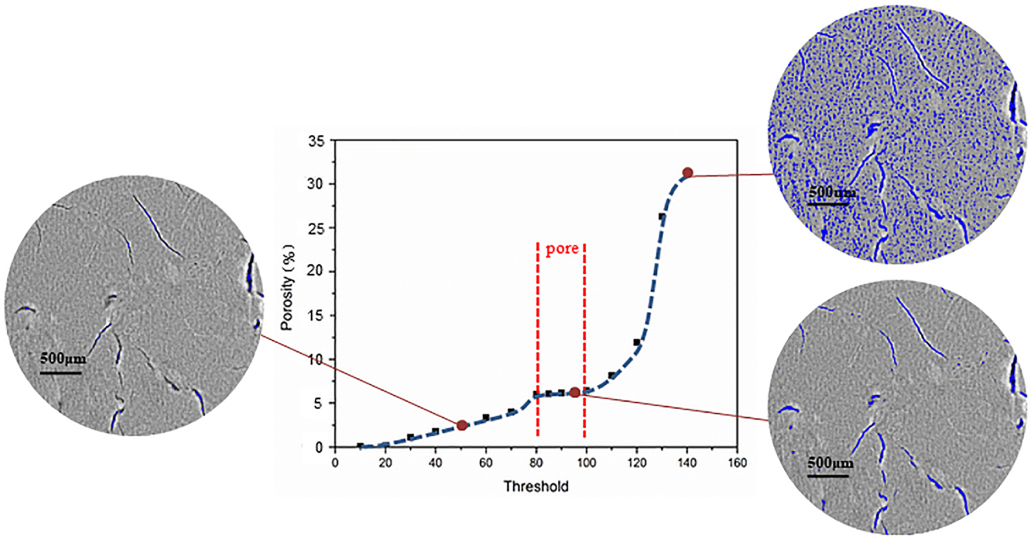

Figure 2

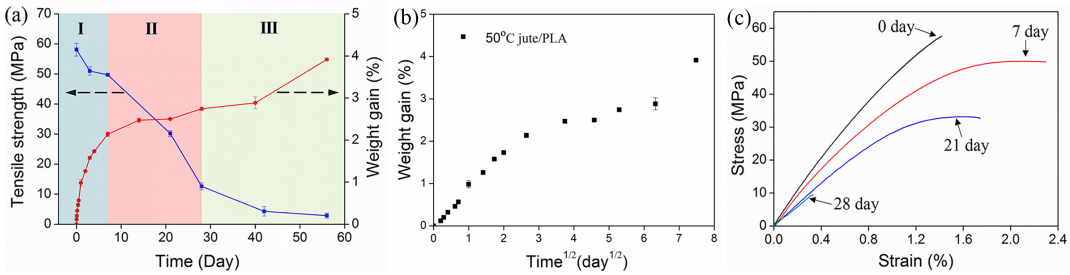
(a)
I
II
III
Tensile strength (MPa)
Weight gain (%)
Time (Day)
(b)
50°C jute/PLA
Weight gain (%)
Time^1/2(day^1/2)
(c)
0 day
7 day
21 day
28 day
Stress (MPa)
Strain (%)

Figure 3

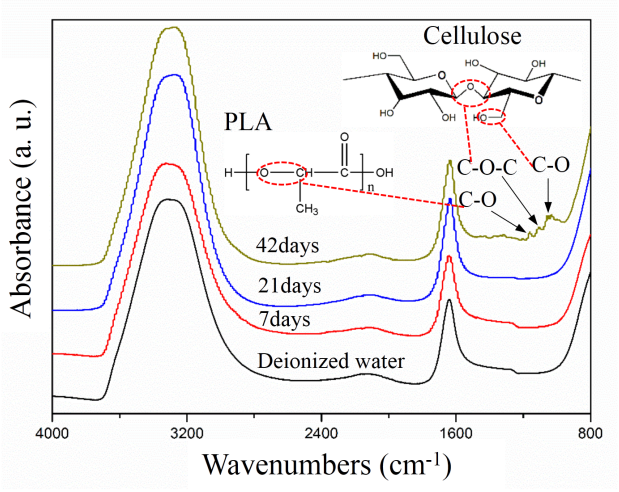

Figure 4

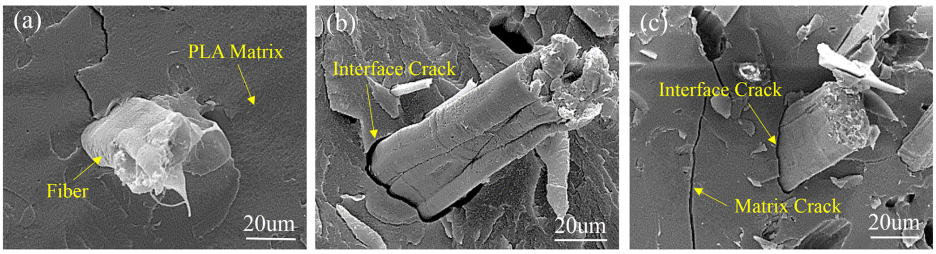

Figure 5

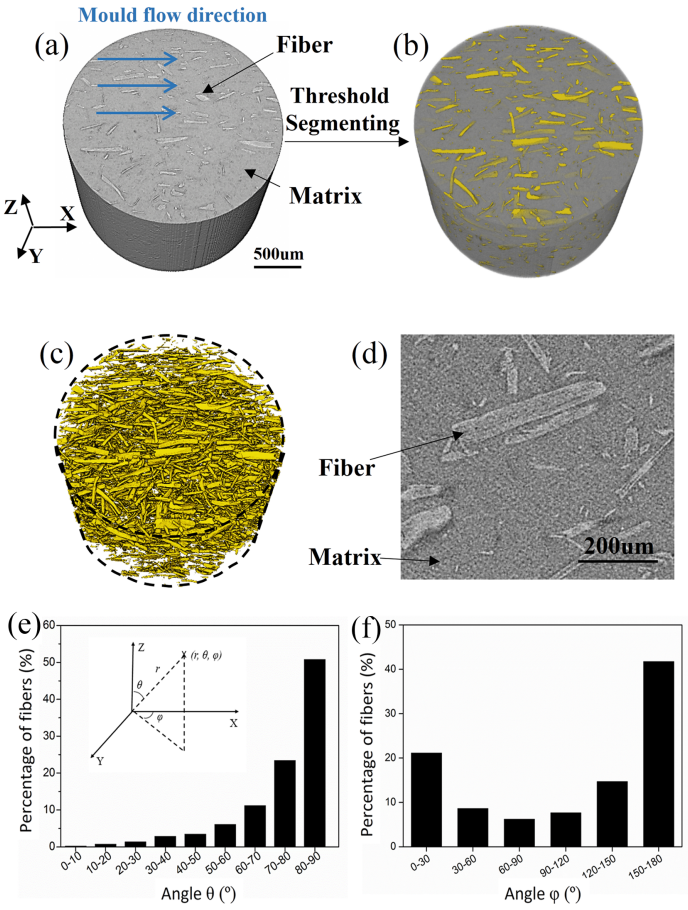

Figure 6

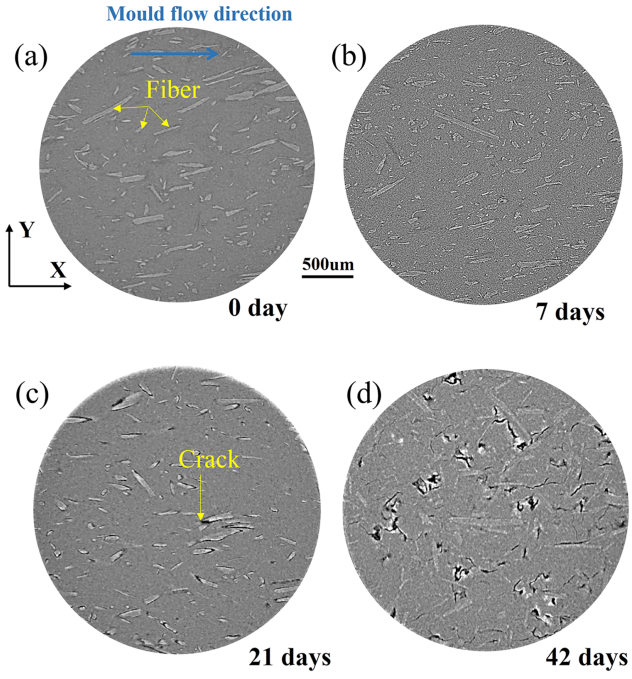

Figure 7

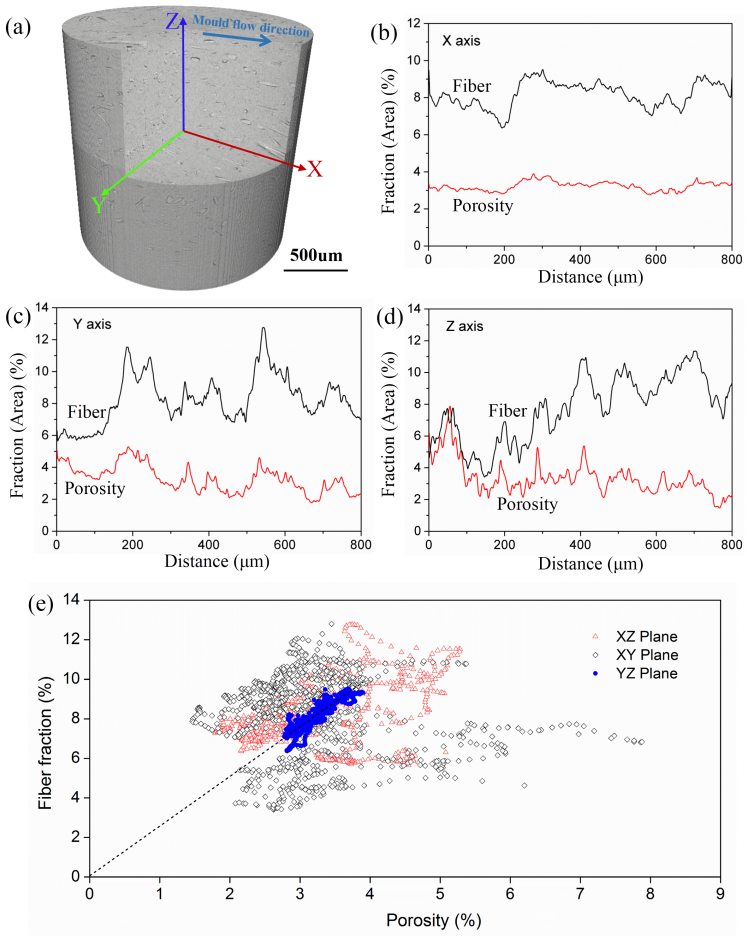

Figure 8

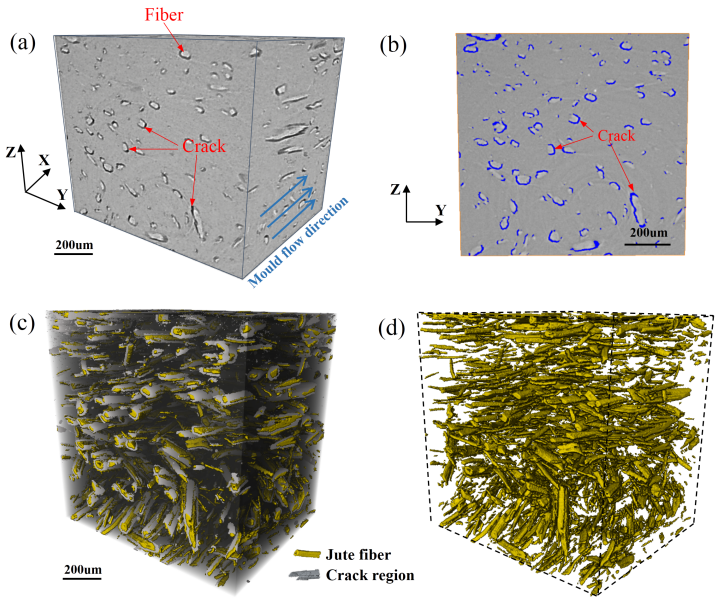

Figure 9

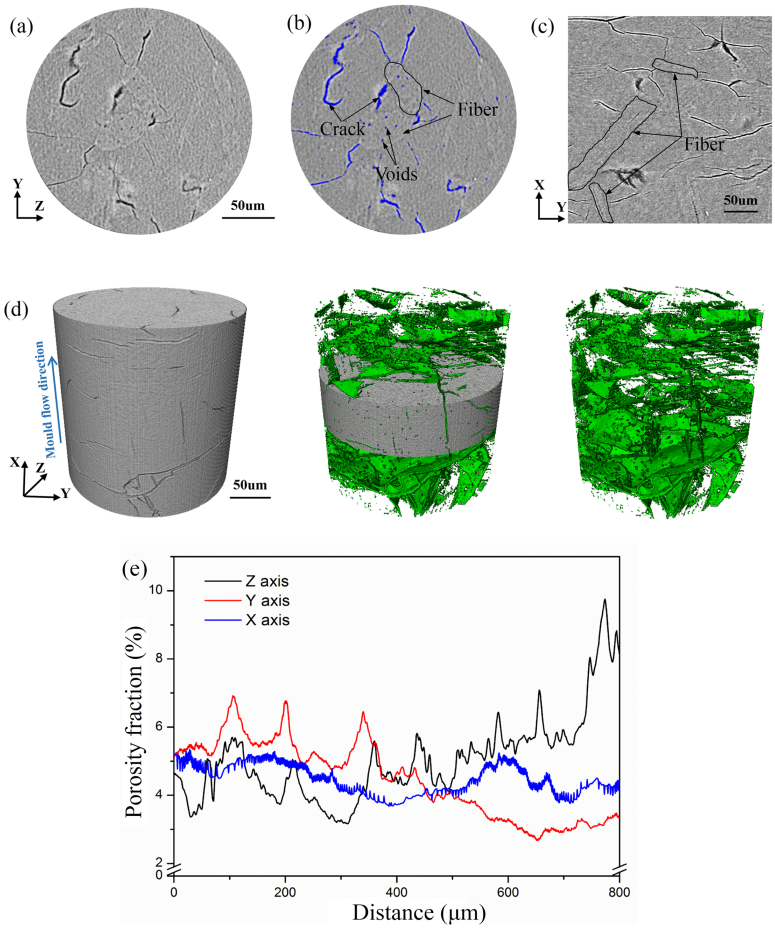

Figure 10

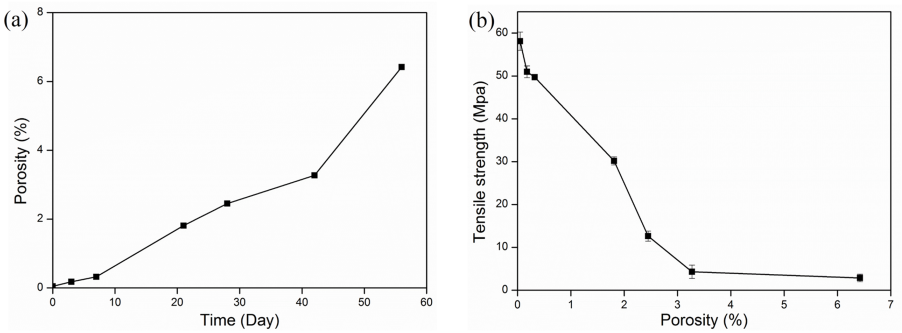

Figure 11